LA-UR- 89-4165

CONF-8908154--20

Rec

JAN 0 8 1990

Los Alamos National Laboratory is operated by the University of California for the United States Department of Energy under contract W-7405-ENG-36

LA-UR--89-4165

DE90 004846

TITLE INEX SIMULATIONS OF THE BOEING FEL SYSTEM

AUTHOR(S) Robert L. Tokar, Alexander H. Lumpkin, Lloyd M. Young, Brian D. McVey, Lester E. Thode, K. C. D. Chan, Steven C. Bender, LANL; A. D. Yeremian, D. H. Dowell, A. R. Lowrey, Boeing Aerospace

SUBMITTED TO Proceedings of 1989 International Conference on Free-Electron Lasers, Naples, FL August 28- September 1, 1989

DISCLAIMER

Los Alamos Los Alamos National Laboratory
Los Alamos, New Mexico 87545

INEX Simulations of the Boeing FEL System

R.L.Tokar,L.M.Young,A.H.Lumpkin,B.D.McVey,L.E.Thode,S.C.Bender,K.C.D.Chan,
Los Alamos National Laboratory,Mail Stop E531
Los Alamos,NM 87545

A.D.Yeremian,D.H.Dowell, and A.R.Lowrey,
Boeing Aerospace and Electronics Company,Mail Stop 2R-00
P.O.Box 3999
Seattle,WA,98124

Abstract

The INEX (integrated numerical experiment) numerical model is applied to the 0.6 μm FEL oscillator at Boeing Aerospace and Electronics Company in Seattle, WA. This system consists of a 110 MeV L-band rf linac, a beam transport line from the accelerator to the entrance of the wiggler, the 5.0 meter THUNDER variable taper wiggler, and a near concentric two mirror optical oscillator. Many aspects of the model for the electron beam accelerator and transport line agree with experimental measurements. Predictions for lasing performance are compared with data obtained in May and June,1989 using a mild tapered wiggler. We obtain good agreement with the achieved extraction efficiency, while 1D pulse simulations reproduce the observed sideband instability.

I. Introduction.

The free electron laser (FEL) system at Boeing Aerospace and Electronics Company in Seattle,WA consists of an rf linac, a horseshoe bend, a 5.0 meter tapered wiggler, and an optical resonator [1]. Previously, we reported simulations of this system using idealized electron beams[2,3]. In this paper, we describe our recently developed end-to-end numerical model of the system and illustrate typical simulation results. In addition, we compare the simulation results with lasing data. The data was obtained in May and June of 1989 with a mild tapered wiggler (4% resonant energy loss) and a near concentric two-mirror optical oscillator. A discussion of data obtained at Boeing in late 1988 and early 1989 with the 5.0 meter uniform wiggler is also available[4], as are recent simulation results for the Boeing FEL using a ring optical resonator, the resonator scheduled for operation in late 1989 [5].

For the Boeing system, the model uses an upgraded version of the accelerator and beam transport code PARMELA , together with the code FELEX [6], a 3D FEL physics code with optical pulse effects and oscillator optics. These codes have been coupled via a third code, refered to as the "translator", and the three codes running together are known as INEX (integrated numerical experiment). Other versions of INEX, employing additional codes, are operational on other systems (e.g.see [7]). In addition, when enhanced optical frequency resolution is required, we employ 1D FEL pulse simulations, initialized to agree as closely as possible with the INEX model of the electron beam.With these models,we obtain good agreement with optical lasing data. For example, with the tapered wiggler configuration, INEX predicts an extraction efficiency of about 1.25% at 0.6 μm wavelength, with the experiment achieving nearly 1.0%. In addition, the 1D modeling predicts the development of sidebands at about the power levels and wavelengths observed in the experiment. It is found that the sideband instability degrades the extraction efficiency by about 25%.

In the INEX model,emphasis is placed on performing the simulations with input parameters based on experimental data. This is particularly important in the accelerator and beam transport systems to obtain agreement with optical lasing data. For example, the relative accelerator and buncher phases are tuned to yield pulse widths, charge transmission, beam energy and energy spread, and beam emittance within the error bars of experimental measurement. The initial charge at the thermionic gun, currents driving solenoidal focussing fields, and power levels in the bunchers and accelerators are all in close agreement with the experiment. After the accelerator, the beam transport system consists of a FODO array, a 180 degree horseshoe bend, and a series of quadrupoles in front of the wiggler for steering the beam and adjusting its size and divergence for matching to the wiggler. In the model, all currents driving these quadrupoles and dipoles are set in PARMELA at the levels measured in the experiment. In addition, the matching of the INEX beam to the wiggler is performed as in the experiment. This produces the most realistic beam possible for use in FELEX.

The INEX modeling approach is particularly attractive for future large systems because it can be used in a problem solving mode to enhance performance. For example, for the Boeing system stability requirements for rf power and phase levels are defined in terms of

their effect on lasing power levels. This procedure determines whether or not the accelerator control system is adequate. In addition, possible performance enhancing hardware changes can be investigated with the model. As one example, INEX predicts significantly less beam emittance growth due to transport around the horseshoe bend will occur if the beam waist at the bend entrance is reduced from that typically exiting the accelerator. If this emittance growth is reduced, INEX predicted that, for the tapered wiggler discussed here, the optical power would increase at least a factor of two. INEX was used to test the idea that the focus/defocus quadrupoles in the FODO array could be driven at different current levels to achieve the required focusing. The beam is now routinely focussed by the FODO array, and the reduced emittance increase due to transport around the 180 degree bend has contributed to enhanced optical power output.

II.The Accelerator and Beam Transport to the Wiggler

An overview of the system modeled in INEX is shown in Figure 1. After the beam exits the accelerator, it enters a FODO array that transports it to the entrance of the 180 degree horseshoe bend. After transiting the bend, it enters a beam transport line referred to as the C-Leg, where it is steered and focused, with its size adjusted for proper wiggler matching. In this section, we will briefly describe the numerical model for the accelerator and beam transport system and discuss the electron beam properties from the electron gun to the entrance of the wiggler. More detailed descriptions of the accelerator and its modeling with PARMELA can be found in [8] and [9].

A. The Accelerator

The rf linac for the Boeing FEL system is a 110 MeV 1.3 GHz machine with a thermionic electron gun, two subharmonic bunchers at 108 and 433 MHz, and a tapered phase velocity buncher at 1.3 GHz. There are six accelerators, with the beam energy increasing from about 3.0 MeV at the entrance of accelerator 1 to about 110 MeV at the exit of accelerator 6. In the simulations, a gaussian current profile is initiated at the gun with a total charge of about 5.7 nC. The electric fields within the gun,bunchers and accelerators used by PARMELA are obtained from the cavity geometries and SUPERFISH [10]. The powers driving the bunchers and accelerators are set to the experimental values, with the field phases tuned to give the experimental charge transmission and other measured beam parameters.

Figure 2 illustrates the energy profile for a typical electron micropulse. Although this is the energy distribution at the wiggler entrance, it is nearly identical to the distribution at the exit of accelerator 6. Plotted is the electron $\gamma\beta_z$ as a function of position within the micropulse. About 3.7 nC exists within the range of longitudinal position shown in the figure. For this charge, the current within the micropulse peaks at about 300 A, and is above 200 A for about 10 ps. This 10 ps width (between about z=0.0 and z=0.3 cm) is the important part of the pulse for generating light via the FEL interaction. The trailing electrons for z<0.0 cm are produced during the bunching process. Carefull tuning in PARMELA can reduce the number of these electrons, but there is no diagnostic in the experiment to tune at this level. In figure 2, variations in the electron beam energy through the 10 ps of about 0.5% are evident, as is the small approximately 0.25% local energy spread. The normalized emittances for the micropulse at the exit of the accelerator are RMS values of $\epsilon_x=\epsilon_y=20\pi$ mm-mrad. The current and energy profiles are relatively unchanged by transport around the bend to the wiggler, but the emittance values are altered.

B. The FODO Array and the 180 degree bend

The FODO array, an array of 10 focusing and defocusing quadrupoles, transports the beam from the exit of the accelerator to the entrance of the bend. If the quadrupoles in the FODO array are driven at equal currents, with a group of 5 at one polarity and the second group of 5 at the opposite polarity, this array does not significantly affect the beam parameters. However, it is advantageous to modify this array to achieve net beam focusing.

Properly tuned,the 180 degree bend is a first order achromatic horseshoe employing four dipoles and 14 quadrupoles. From the perspective of its effect on the FEL interaction, we are interested in how this bend changes the electron beam parameters due to the transport. With PARMELA, the effect on beam charge,arrival time, pointing and transverse position at the wiggler have been investigated as a function of beam energy. The changes in beam energy from micropulse to micropulse are due, for example, to an imperfect accelerator control system and are often observed in experimental stripline beam position monitor data. It is found that the bend is nearly isochronous over a range of about +/- 0.5 MeV, with about 1.0 to 2.0 ps maximum arrival time error. Charge transmission over this range is nearly 100%. Energy variations of this magnitude also lead to pointing jitter and transverse position jitter at the wiggler entrance. This jitter can not be corrected on the time scale shorter than a macropulse length, about 100 μs. For the +/- 0.5 MeV energy range, pointing angles are about +/- 0.02 mr and transverse offsets are a few tenths of mm. Although these effects are not discussed in detail in this paper, they have been investigated with FELEX and with 1D pulse simulations and lead to longer start-up times and reduced saturated extraction efficiency.

Although these effects are important, they do not seriously degrade the FEL system if the bend is properly tuned and the accelerator control system is within tolerance. As we will see, experimental data suggests this has been achieved. Therefore, the most important effect of the horseshoe bend on the electron beam is the increase in beam emittance produced due to the transport. A substantial increase in emittance can seriously degrade the FEL performance due to a reduction in the beam brightness. The increase reduces both the small signal gain and the saturated extraction efficieny, thus defining the maximum FEL performance. Using PARMELA, it is established that the increase in the emittance due to transport around the bend is the quadrature sum of uncorrelated emittance contributions due to the effects of non-linear forces, space charge forces, and forces due to wakefields. The wakefield effects in the bend are calculated using TBCI [11] and the known shapes of wakefield generators (e.g. bellows and striplines). The present model has 16 wakefield generating stations within the bend. Of the three forces, only the wakefield effects are dissipative, enabling the density in phase space along an electron trajectory to change. The non-linear and space charge forces can change the projected RMS x and y emittances, but not the total volume in phase space.

Using K-V distributions [12] in PARMELA, the following scaling relationship has been empirically determined for the horseshoe bend:

$$\varepsilon_{out,x}=(\varepsilon^2_{in,x} + \varepsilon^2_{t} + \varepsilon^2_{sc} + \varepsilon^2_{w})^{1/2} \qquad (1a)$$

and

$$\varepsilon_{out,y}=(\varepsilon^2_{in,y} + \varepsilon^2_{t})^{1/2} \qquad (1b)$$

with

$$\varepsilon_t = 41\pi\delta E(r_e/2.0)^2 \qquad (1c)$$

$$\varepsilon_{sc} = Q/3.5(45\pi + 35\pi(r_e-2)) \qquad (1d)$$

$$\varepsilon_w = Q/3.5(37\pi + 15\pi(r_e-2)). \qquad (1e)$$

The direction x is the horizontal bend plane, the direction of energy dispersion produced by the dipoles, while y is the vertical direction, with no energy dispersion. In these equations, all emittances are RMS values ,$\varepsilon_{in,x}$ and $\varepsilon_{in,y}$ are the x and y emittances at the entrance of the bend, δE is the full energy spread of the beam in MeV, r_e is the edge radius of the beam at the bend entrance in mm, and Q is the total charge in the micropulse, in nC. We assume a fixed micropulse length, providing a scaling with Q rather than current. The quantities ε_t, ε_{sc}, and ε_w are the emittance contributions due to the non-linear transport effects, space charge effects, and wakefield effects. Note that if $\delta E=0$ and we neglect the space charge and wakefield contributions, there is no emittance increase. Liouville's theorem requires this because the RMS emittance is proportional to the total phase space area for a K-V distribution. Equations 1 were obtained for the ranges $0.0<\delta E<2.0$ MeV, $0.5<r_e<3.0$ mm, and $0.0<Q<7.0$ nC. Note that the space charge term must be modified with an additional 1/r term to apply for $r_e<0.5$ mm. We find similar scaling relationships for other bends in FEL systems.

The utility of equations 1 is to provide experimental direction toward a performance increase. For the electron beam parameters corresponding to Figure 2, $\varepsilon_{in,x}=\varepsilon_{in,y}=20\pi$, Q=3.7nC, and δE is about 0.5 MeV. For these parameters and r_e=2mm, the typical beam radius at the exit of accelerator 6, equations 1 yield $\varepsilon_{out,x}=68\pi$, and $\varepsilon_{out,y}=29\pi$. In contrast, if we can focus the electron beam before entering the bend to achieve r_e=1mm, $\varepsilon_{out,x}=33\pi$ and $\varepsilon_{out,y}=21\pi$. FELEX predicts that reductions in the x emittance of this magnitude can increase the FEL saturated extraction efficiency by at least a factor of two for the 5.0 meter tapered wiggler discussed in this study. Therefore, it is desirable to focus the beam before entering the bend, and this is accomplished by modifying the FODO array so that the two groups of focus and defocus quadrupoles are driven at different current levels. This procedure is now routinely performed in the experiment.

C. The C-Leg, Steering and Matching

After transiting the bend, the beam must be steered into the wiggler and its transverse size and divergence must be adjusted to achieve proper wiggler matching. This is ac-

complished in PARMELA and in the experiment with steering coils and two quadrupole triplet sets in the beam transport line in front of the wiggler (see Figure 1). One of the triplet quadrupoles within the C-Leg is varied to obtain a waist at an optical transition radiation screen[13] upstream of the wiggler. The quadrupole settings and beam waist sizes are given to the code TRANSPORT to determine the triplet settings for proper wiggler matching. It should be noted that this procedure also yields experimental ϵ_x and ϵ_y values, providing a further check on the diagnostics and model.

Figure 3 illustrates the electron beam envelope within the wiggler before and after the matching procedure. In the top frame, the beam has not been steered or matched. Note that it arrives at the wiggler entrance about 1.0 mm displaced in the y direction. This, together with the non optimum transverse size and beam divergence, produces large oscillations in both the position and size of the beam through the wiggler. With this beam in FELEX, the FEL will not start up due to significant aperturing of the optical field by the wiggler tube at the exit of the wiggler. In contrast, the bottom frame illustrates the beam envelope after the steering and matching procedure. Note that the beam arrives nearly on axis, with the beam centroid remaining near the wiggler axis throughout the transport. The beam exhibits some sausaging even after the matching procedure, because the emittance varies as a function of position within the electron pulse and the matching procedure has experimental error [13]. This beam does not lase in FELEX, as will be discussed in the next section.

III. Simulations of Lasing Performance and Comparison with Data

A.) Simulation Results

In this section, we describe FELEX simulations of lasing using the PARMELA beam and 1D pulse simulations of the sideband instability.The FELEX simulations are perfonned for a near concentric two mirror resonator, with a cavity loss of 7.5%. This loss value is consistent with experimental measurements of ringdown in May and June,1989. The wiggler is the 5.0 meter THUNDER wiggler [14], configured to have a 1.25 m uniform section together with a 3.75 m linear taper in magnetic field strength. The degree of taper corresponds to about a 4% decrease in the resonant electron energy. Therefore, for this wiggler, we estimate an idealized extraction efficiency near 2.0%, if half the electrons are trapped in the pondermotive well. As we will see, the experiment has approached 1.0%, with the optical power still increasing at the end of the macropulse.

Figure 4 illustrates the current and emittance of the micropulse at the entrance of the wiggler. This micropulse is steered and matched, with the envelope through the wiggler plotted in the bottom panel of Figure 3. Within the 10 ps high current region of the micropulse, between about z=0.0 and 0.3 cm, the 90% emittance is about ε_x=140π and ε_y=100π. This corresponds to RMS values of about 35π and 25π respectively. Note that $\varepsilon_x > \varepsilon_y$ after the bend, due to the space charge and wakefield contributions of equations 1. The emitance has increased from its pre bend x and y values of 20π indicating that, for the notation of equations 1, ε_t=15π and $(\varepsilon^2_{sc}+\varepsilon^2_w)^{1/2}$=25$\pi$. These numbers are in good agreement with the beam radii and energy spread in INEX. In the experiment, the beam is often focussed by the FODO array to radii near 1 mm, and the pulse averaged energy spread is near 0.5 MeV.

Results from FELEX, obtained with the beam in Figure 4, are shown in Figure 5. This multi-pass oscillator simulation uses the Figure 4 beam on every pass, neglecting pulse to pulse variations. To limit the computational time, the simulation was started near saturation, with the optical pulse after 25 passes shown in Figure 5. In the top frame is a perspective plot of the optical electric field magnitude at the exit of the wiggler in the transverse (x) and longitudinal (z) planes. The peak electric field strengths are about 6×10^4 statV/cm. In the bottom frame is the extraction efficiency as a function of z, the position within the micropulse. FELEX predicts a small signal gain for this beam of about 200 to 300% and a saturated pulse averaged extraction efficiency of 1.25%. Recent experimentally measured small signal gains from late July,1989, are as high as 200%, although the average small signal gain over many passes is about 50%, due, for example, to accelerator control system problems during the small signal portion of the macropulse. The z dependance of the extraction efficiency can be compared to the energy distribution, current and emittance as a function of z shown in Figures 2 and 4. Note that the peaks in extraction efficiency are near the peaks in current, and that peak extraction above 2.5% is achieved, indicating localized regions of strong FEL interaction.

For the electric field strengths of the laser pulse in Figure 5, 3 to $6x10^4$ statV/cm, the spatial period for synchrotron oscillations ranges from about 150 to 110 cm (e.g.see [15]). Therefore, in this simulation the electrons perform about 3 to 5 sychrotron oscillations in the 5 meter 230 period THUNDER wiggler, and the system should exhibit sidebands at wavelengths about 1.5 to 2 0% larger and smaller than the fundamental. However,due to limited computational resources, the FELEX simulations follow a limited number of optical wavefronts (24 in Figure 5) and do not have the bandwidth to investigate the sideband instability. We perform 1D FEL pulse simulations,as in [2], to investigate the development of the instability and how much it degrades the FEL performance with the mild tapered wiggler. Many of these simulations have been performed, here we discuss a few representative examples. The pulse widths in the simulation illustrated here is in close agreement with the INEX pulse in Figure 4, and the energy spread has contributions from both the real (0.3% at the 1/e point) and emittance (about 1.0%) components. The current is 200 A, and yields peak small signal gains of about 100%. The simulation saturates at about 6.0 GW in the optical cavity, with an extraction efficiency of about 1.7%. This extraction efficiency is larger than the INEX result, primarily because an idealized electron beam is used in the pulse simulation.

There are at least two important results from the pulse simulations. The first is that the sidebands do develop as expected. At the power levels shown in Figure 5, sidebands are present, with the strongest instability at wavelenths about 1 to 2% larger than the fundamental. At intermediate power levels, sidebands develop at wavelengths closer to the fundamental but these,as well as shorter wavelength sidebands, do not attain large amplitudes. The second point is that the development of the sidebands does not seriously degrade the extraction efficiency over at least 400 simulation passes. Because the experiment is limited to about a 100 μs macropulse, or about 400 micropulses, this result suggests the instability will not seriously degrade the experimental performance. This is in contrast to the effects of sidebands on this system with a strongly tapered wiggler [2].

However, the pulse simulations do indicate that the extraction efficiency is lower than that obtained with sideband suppression. In addition, the outcoupled power will show signatures of sideband development. These points are illustrated in Figure 6, where extraction efficiency as a function of pass and three optical spectra are shown from the pulse simulation. The simulation attains an extraction of about 1.7%, while the identical simulation with ideal grating rhomb sideband suppression as in [2] attains an efficiency of 2.3%. This indicates about a 25% reduction in extraction due to the instability. The spectra in Figure 6 are at pass 30, 50, and 90, the positions marked A,B,and C in the plot of extraction efficiency. Note the flattening of the extraction efficiency, or equivalently outcoupled energy, near the point B in Figure 6. This flattening is at the position where the fundamental wavelengths, around 640 nm, are no longer increasing in intensity while the long wavelength sidebands are beginning to grow. The flattening in extraction is due to the evolution of the optical bucket in this region, leading to less efficient trapping. The third spectra, at pass 90, illustrates the growth of the sideband to intensities equal to the fundamental. Later spectra show that the FEL even-

tually chirps completely over to the sideband wavelengths, where saturation occurs.

B. Comparison with Data.

The simulations yield predictions of the laser extraction efficiency, with the 1D pulse simultions predicting the development of the sideband instability. The various simulation numerical models achieve extraction efficiencies of 1.25 (INEX,no sidebands), 1.7 (1D pulse with sidebands), and 2.3 (1D pulse with sideband suppresion) percent. In the experiment, there are two methods of determining the extraction efficiency: 1.) from measurements using a silicon detector of outcoupled laser energy and a knowledge of electron beam and oscillator parameters, and 2.) from electron spectrometer measurements during lasing and non-lasing periods.

Examples from the first method are illustrated in Figure 7, where extraction efficiency versus shot number (time) is plotted for 39 lasing macropulses on May 17,1989. The individual shots are separated in time by about 1.0 minute, and were chosen at random from the large lasing data base for this day. The extraction efficiencies are calculated using the approximate equation

$$\eta=(L/T)(E_0/E_{eb})$$

where L is the cavity loss, T is the mirror transmission, E_0 is the peak energy measured at the detector, and E_{eb} is the energy of the electron beam. The peak energy always occurs near the last lasing micropulse in the macropulse, immediately before the termination of the electron beam. The measured electron beam parameters are total charge equal to about 2.5 nC and a mean energy of 110 MeV (E_{eb}=275 mJ). The outcoupling through the oscillator mirrors to the detector is known to be about 0.4% at a wavelength of 650nm, while the cavity losses are inferred from ringdown measurements to be about 7.7%. Typical energies at the silicon detetector are around 100 μJ, with the highest observed energy to date of 138 μJ. Experimental uncertainty in the inferred extraction is about +/- 25%, primarily due to the uncertainty in the cavity ringdown and charge measurements. In Figure 7, we assume the above electron beam and oscillator parameters, measured on May 17,1989, apply to all 39 macropulses, neglecting shot to shot variations. The figure illustrates that often the experiment performs at levels below the simulation predictions, but on occasion all system parameters are tuned to yield performance near 1.0% extraction efficiency. For example, in the 40 minute period of Figure 7, for about 20 minutes the system tune was sufficient to achieve 0.5 to about 1.0% extraction. Also shown in Figure 7 is the INEX 1.25% prediction. It is interesting to note that if we apply a 25% correction for the sideband instability, obtained from the 1D pulse simulations, to the INEX 1.25% average value, we obtain 0.9%, about the highest extraction in Figure 7.

Further support for operation at extraction near 1.0% is in Figure 8, which illustrates experimentally measured electron spectra both during lasing and non-lasing periods. These spectra are integrated over about 160 micropulses. Trapped decelerated electrons are visible, extending to 4% below the mean energy, in agreement with the wiggler taper. Analysis of the

centroid shift yields an extraction efficiency of η=0.8+/-0.2%, in good agreement with the simulation predictions. It should be noted that the spectrograph resolution is about 1.4%, although the centroid shift can be measured to about 0.2%. Therefore, the energy spread in Figure 8 is not the single micropulse energy spread. This energy spread is always less than 1%, due to an energy collimator in the horseshoe bend.

Figures 9 and 10 illustrate observations of the sideband instability, obtained with a streak spectrometer system in May,1989. The top panel displays an intensity scatter plot of wavelength vs. time for a 125 μs macropulse. It should be noted that 125 μs is about 600 passes through the wiggler. At early times, the fundamental wavelengths are visible, with a center wavelength of about 650 nm. At about t=50 μs, or 200 oscillator passes, the longer wavelength sidebands are begining to grow. The bottom panel illustrates intensity vs wavelength through the times corresponding to the horizontal window in the top panel. The fundamental is visible and centered about 650 nm, with the long wavelength sideband centered about 663 nm. In addition, a closer wavelength sideband is visible at about 659 nm, although it does not attain large amplitude. Figure 10 is in the same format as Figure 9, but the intensity vs wavelength in the bottom panel is late in the macropulse, with the horizontal analysis window at about t=80 μs. By this time, the sideband has become the dominant wavelength, with the intensity at the fundamental decaying away. This behavior is like that observed in the 1D pulse simulations, although the time scale is longer (see below), and occurs at comparable intracavity power levels. Although it is not clear from Figure 10, the optical power is still increasing at the end of the macropulse.

The final point is the predicted decrease in trapping efficiency when the sidebands began to grow (Figure 6,point B). Observations of this decrease are shown in Figure 11. Plotted is extraction efficiency vs. time inferred from outcoupled laser energy measured with the silicon detector. The data is over the entire macropulse, with the extraction fall off near 100 μs at the point where the electron beam ends. It is clear from this figure that the power is still climbing immediately before this point. The flattening of the extraction is observed around 50 μs, or at about pass 200. This is the position in the macropulses where the streak system first observes the sideband growth. However, it should be noted that the time scale for sideband development is about 4 times longer in the experimental data than it is in the simulation. This is due to the lower average small signal gain observed in the experiment, a consequence of, for example, electron beam energy variations from micropulse to micropulse, non-optimum tuning of the beam transport system, non ideal matching to the wiggler, and non ideal steering of the electron beam within the wiggler. These effects can be included in INEX, but the Cray X-MP CPU time required is very large.

IV.) Conclusion

The INEX end-to-end simulation model is operational on the FEL system at Boeing. The comparison of experimental data and simulation for a mild taper wiggler yields good agreement for the extraction efficiency and the development of the sideband instability. INEX is frequently used in a problem solving mode to aid the experimentalists, and has also been used to identify hardware changes that have enhanced the FEL output. This success of INEX on the Boeing FEL confirms that it will be a valuable tool in the design and operation of future FEL systems.

Acknowledgements

The authors want to thank Bob Justice of EG&G Los Alamos for providing outcoupled energy data and Dave Quimby of Spectra Technology, Bellevue,WA for helpful discussions and comments on an early version of this manuscript. This work was performed under the auspices of the U.S. Department of Energy and was supported by the U.S. Army Strategic Defense Command.

References

1.) Shoffstall,D., "A Visible Wavelength Free Electron Oscillator",Proc. Int. Conf. Lasers, pg. 171,STS Press,McLean,VA,1989

2.) Tokar,R.L.,B.D.McVey, and J.C.Goldstein, "Sideband Suppresion in Free Electron Lasers Using a Grating Rhomb",IEEE J. Quant. Elecs,24,6,856,1988.

3.) Tokar,R.L.,B.D.McVey,L.E.Thode, and G.M.Gallatin, "Simulations of a Ring Resonator Free Electron Laser",IEEE J.Quant.Elecs.,1,73,1989.

4.) Lumpkin,A.H.,R.L.Tokar,D.H.Dowell,A.R.Lowrey,and D.Yeremian,"Improved Performance of the Boeing/LANL FEL Experiment", 1989 International FEL Conference, Naples,FL.

5.) Sun,K.C.,B.D.McVey,and R.L.Tokar,"Resonator Mode Matching for Free Electron Laser Optical Guiding",1989 Inernation FEL Conference,Naples,FL.

6.) McVey,B.D.,"Three Dimensional Simulations of Free Electron Laser Physics", Nucl Inst Meth Phys Res.,A250,449,1986.

7.) Goldstein,J.C.,B.E.Carlsten,and B.D.McVey,"INEX Simulations of the Los Alamos HIBAF FEL/MOPA Experiment",1989 International FEL Conference,Naples,FL.

8.) Adamski, J. et al., "Boeing 120 MeV rf Linac for FEL Research", IEEE Trans. Nucl. Sci.,Vol NS-32 No.5,pg. 3397,Oct,1985.

9.) Yeremian,A.D.,J.Adamski,R.Kennedy,W.Gallagher,J.Orthel,and L.M.Young,"Boeing 120 MeV rf linac Injector Design and Accelerator Performance Comparison with PARMELA, to be published in IEEE Trans. Nucl. Sci.,1989.

10.) Halbach,K., and R.F.Holsinger, "SUPERFISH-A Computer Program for Evaluation of rf Cavities with Cylindrical Symmetry", Particle Accelerators,7,213,1976.

11.) Weiland, T., "Transient Electromagnetic Fields Excited by Bunches of Charged Particles in Cavities of Arbitrary Shape", Proceedings of the 11th Int. Conf. on High Energy Accelerators,Geneva,1980,pp 570-575.

12.) Kapchinsky,I.M.,and V.V.Vladimirsky, Proc. Int. Conf. on High Energy Accelerators and Instrumentation, CERN,1959,p 274-288.

13.) Dowell,D.H.,J.Adamski,A.R.Lowrey, and A.H.Lumpkin,"Optical Transition Radiation as an Electron Beam Diagnostic in the Boeing Visible FEL", Proceedings 1989 FEL Conference, Naples,FL,1989.

14.) Robinson,K.,D.C.Quimby,and J.M.Slater,"The Tapered Hybrid Undulator (THUNDER)

of the Visible Free Electron Laser Oscillator Experiment", IEEE J.Quant Elecs.,QE-23,1497,1987.

15.) Quimby,D.C.,J.M.Slater and J.P.Wilcoxon, "Sideband Suppression in Free Electron Lasers with Multiple Sychrotron Periods",IEEE J.Quant.Elecs,QE-21,979,1985.

Figure Captions

Figure 1.) Schematic layout of the Boeing FEL system showing the accelerator, FODO array, horseshoe bend, wiggler, and optical oscillator.

Figure 2.) Distribution of electron $\gamma\beta_z$ within the electron micropulse used in the simulations. About 3.7 nC of charge is in this micropulse.

Figure 3.) Envelope of the electron micropulse within the 5.0 meter wiggler both before (top panel) and after (bottom panel) the wiggler matching procedure.

Figure 4.) Current and 90% emittance within the electron micropulse used in the multi-pass oscillator simulations. Note that the region of large current ($0.0 < z < 0.3$ cm) corresponds to the region of small energy spread, as shown in Figure 2.

Figure 5.) Perspective plot of the optical electric field magnitude from FELEX in the transverse (x) and longitudinal (z) planes, together with the extraction efficiency as a function of position within the electron micropluse. The laser pulse is plotted at the exit of the wiggler after 25 passes around the resonator and through the wiggler. The extraction efficiency is 1.25%.

Figure 6.) Results from one dimensional simulations to investigate the growth of the sideband instability. Plotted is extraction efficiency as a function of the number of passes through the wiggler together with three optical spectra. The optical spectra are shown at pass 30,50, and 90, with the spectra at pass 90 exhibiting significant intensity at the long wavelength sideband components.

Figure 7.) Extraction efficiency, derived from measurements of outcoupled laser power, as a function of shot number on May 17,1989. The observations are separated by about 1 minute.

Figure 8.) Data froom the electron beam spectrometer after the wiggler measured on June 8,1989. When the system is lasing, trapped decelerated electrons are visible down to 4% below the beam energy, inagreement with the 4% resonant energy taper. Analysis of the data yields extraction efficiency of η=0.8+/-0.2%.

Figure 9.) Data from a streak spectrometer system showing optical spectra versus time in the top panel. The bottom panel is a plot of the optical spectra intensity as a function of wavelength about 50 μs into the macropluse (the horizontal window in the top panel). Note the two sidebands developing at wavelengths larger than the fundamental.

Figure 10.) The same format as Figure 9, but the optical spectra in the bottom panel is later in the macropulse, about t=80 μs. Note that the sideband is now of higher intensity than the fundamental.

Figure 11.) Extraction efficiency as a function of time in the macropulse for two lasing shots

on May 17,1989. The extraction efficiency is inferred from the outcoupled laser power. The flattening in extraction occurs when the sidebands begin to grow, in agreement with the simulations.

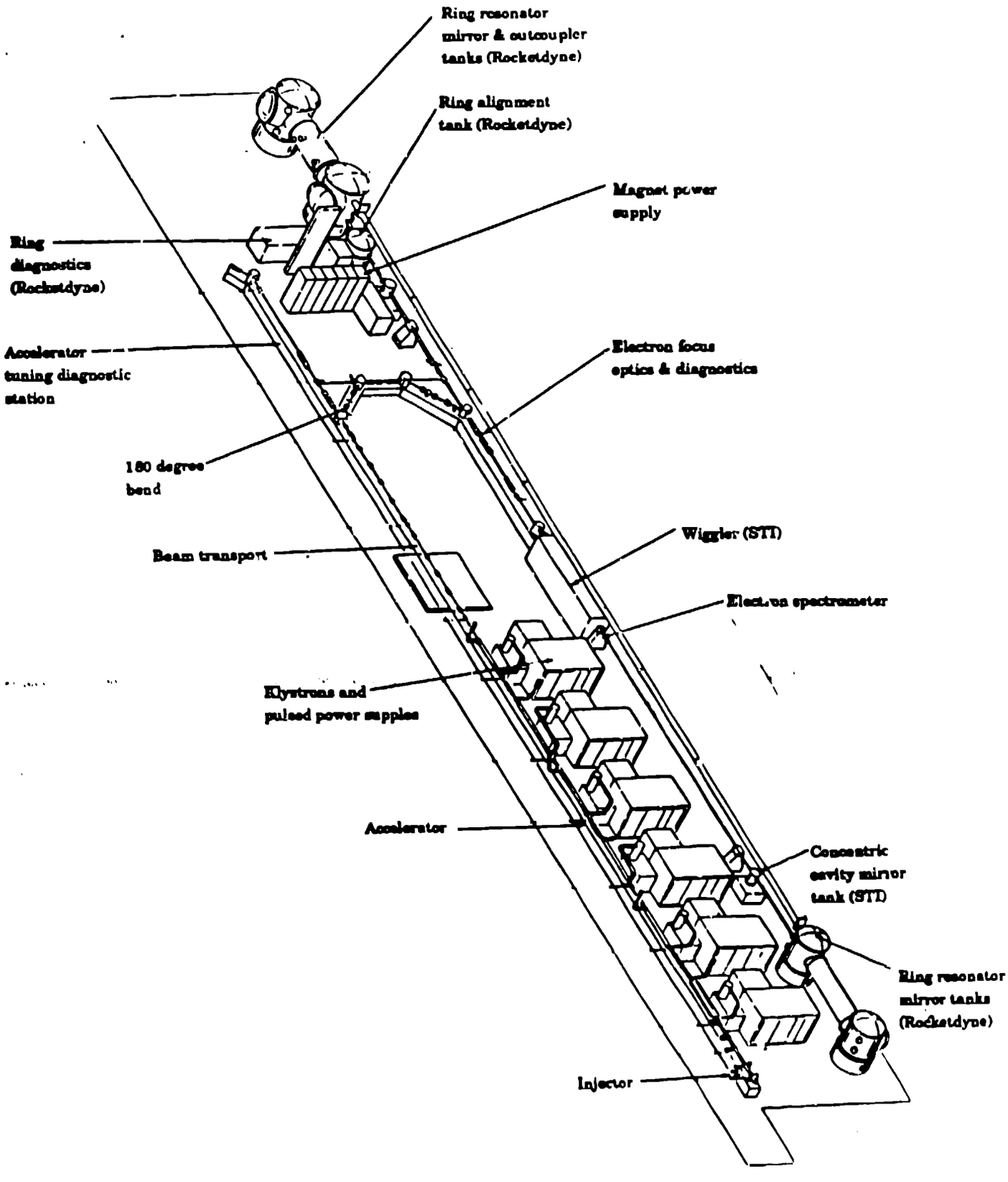

Figure 1◆ Laboratory Layout of FEL Concentric Oscillator and Burst Mode Ring Resonator Experiments

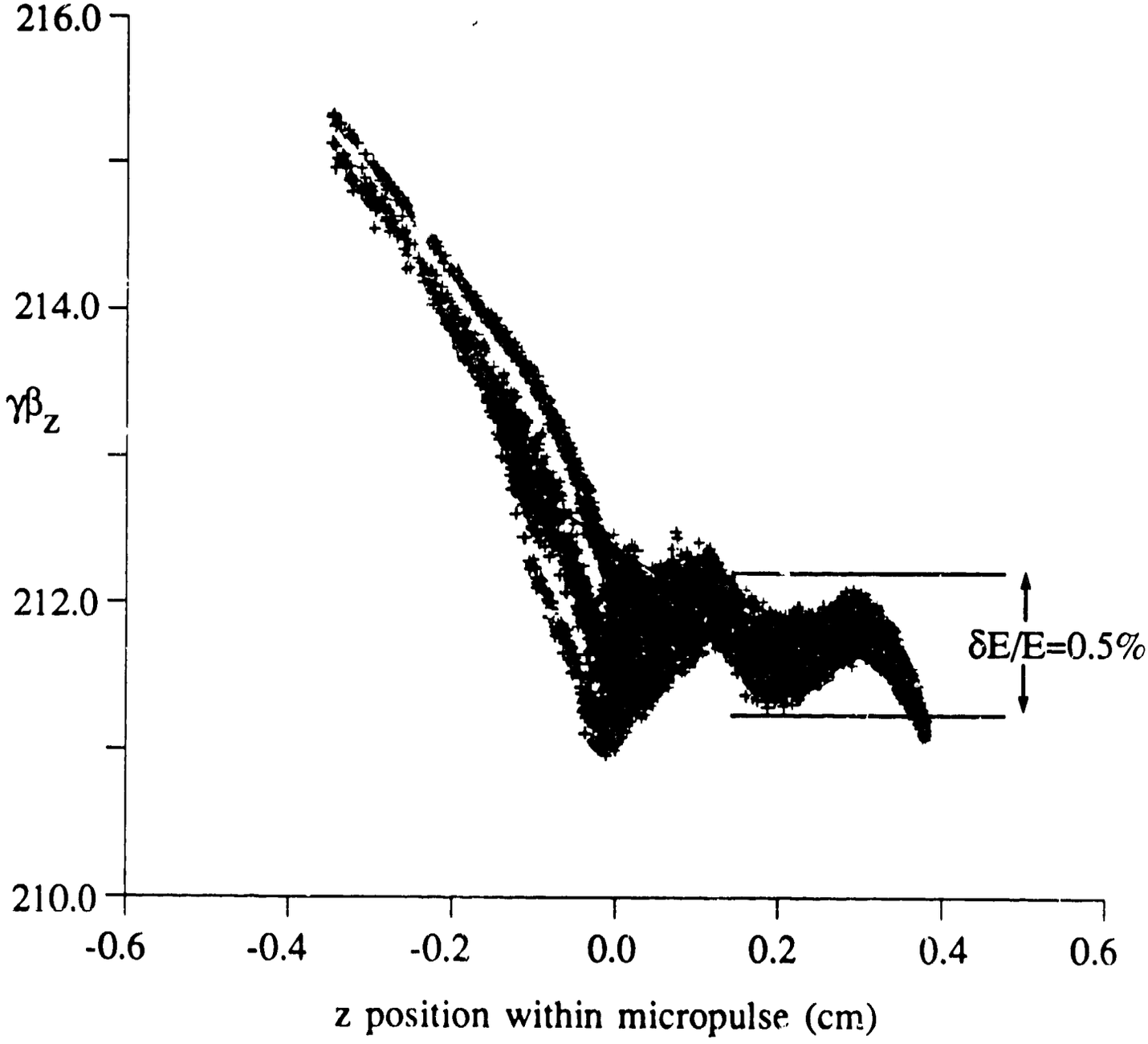
216.0
214.0
212.0
210.0
$\gamma\beta_z$
δE/E=0.5%
-0.6
-0.4
-0.2
0.0
0.2
0.4
0.6
z position within micropulse (cm)

Figure 2

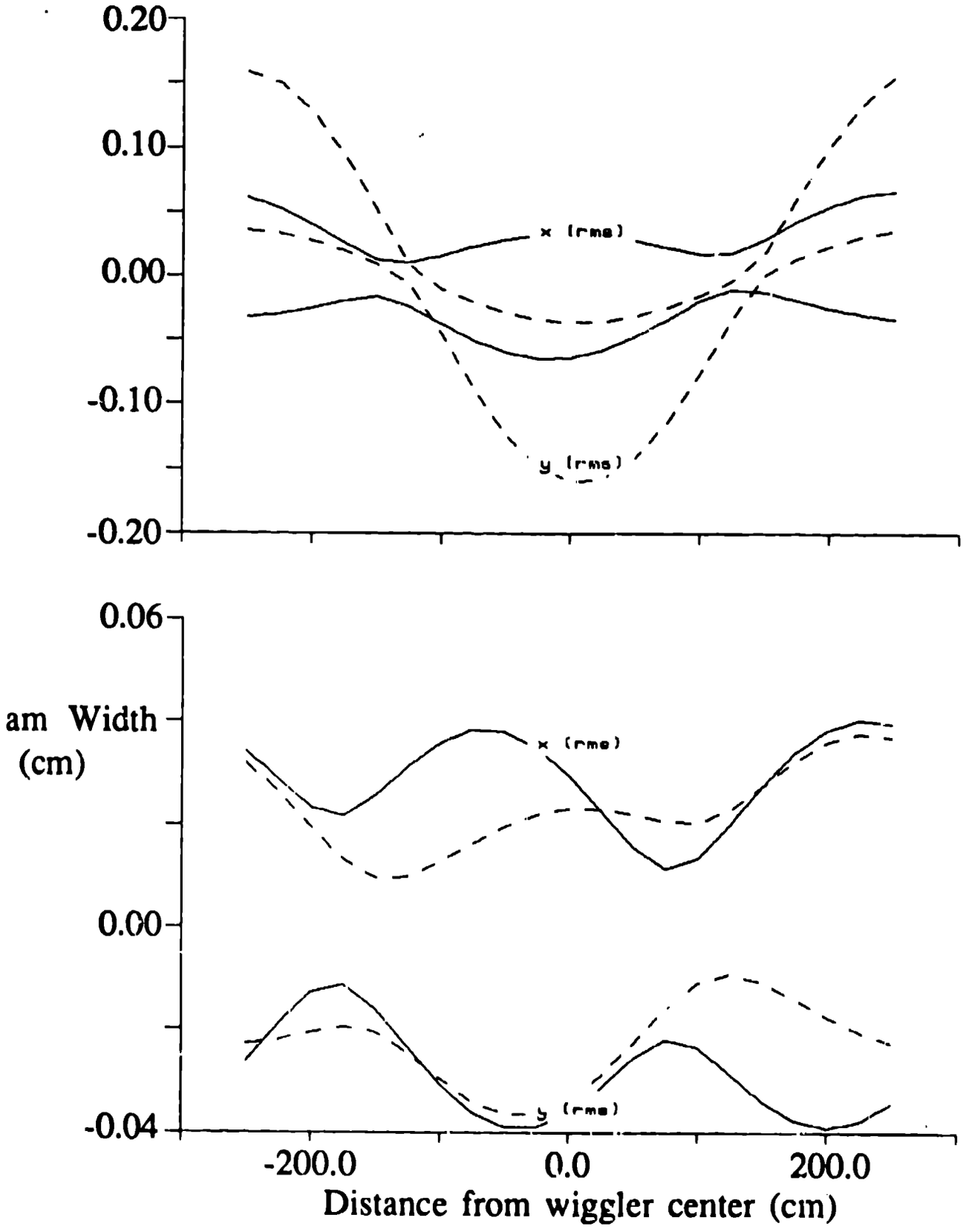
0.20
0.10
0.00
-0.10
-0.20
x (rms)
y (rms)
0.06
am Width
(cm)
0.00
-0.04
x (rms)
y (rms)
-200.0
0.0
200.0
Distance from wiggler center (cm)

Figure 3

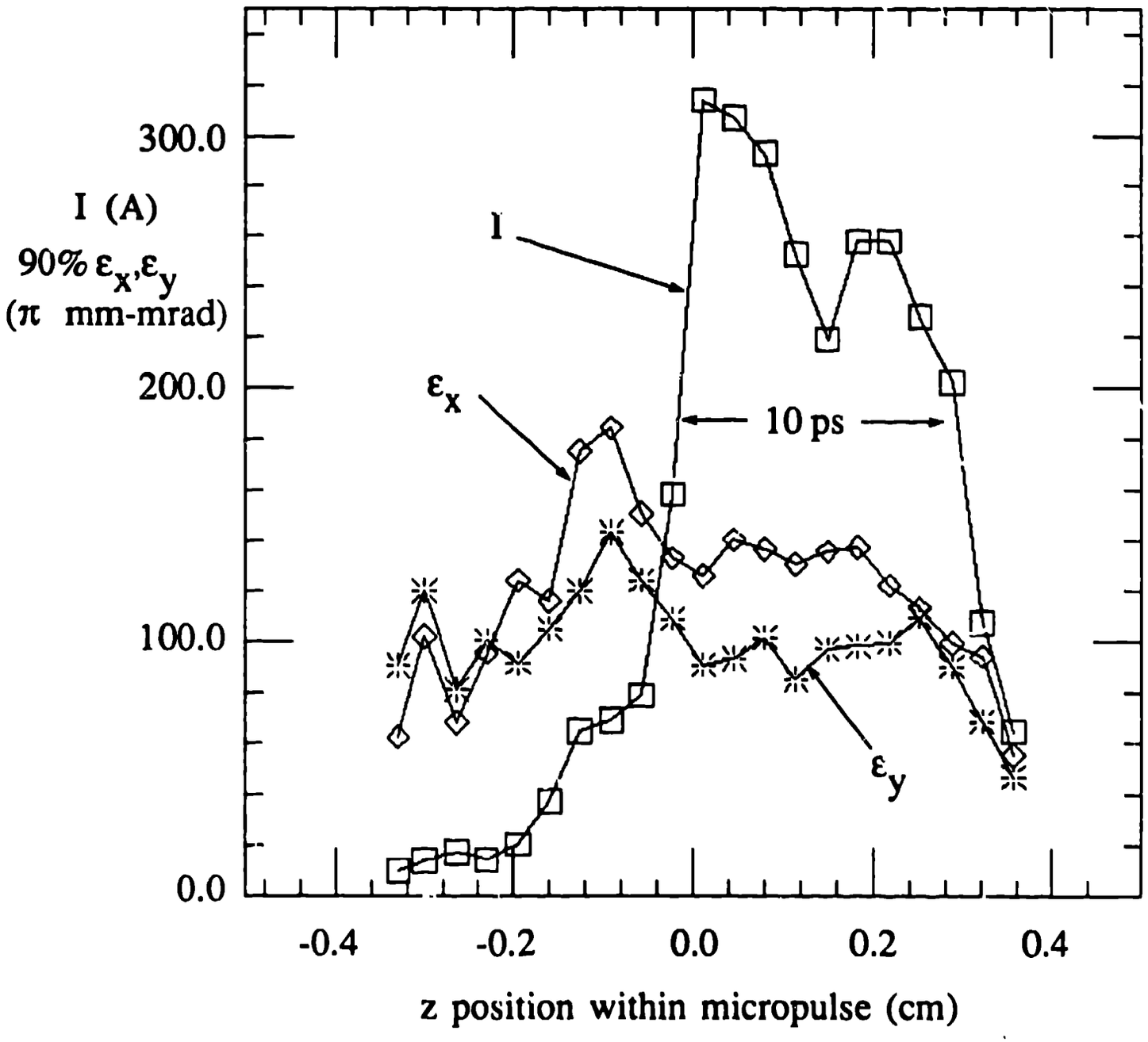
300.0
200.0
100.0
0.0
I (A)
90% ε_x,ε_y
(π mm-mrad)
I
ε_x
10 ps
ε_y
-0.4
-0.2
0.0
0.2
0.4
z position within micropulse (cm)

Figure 4

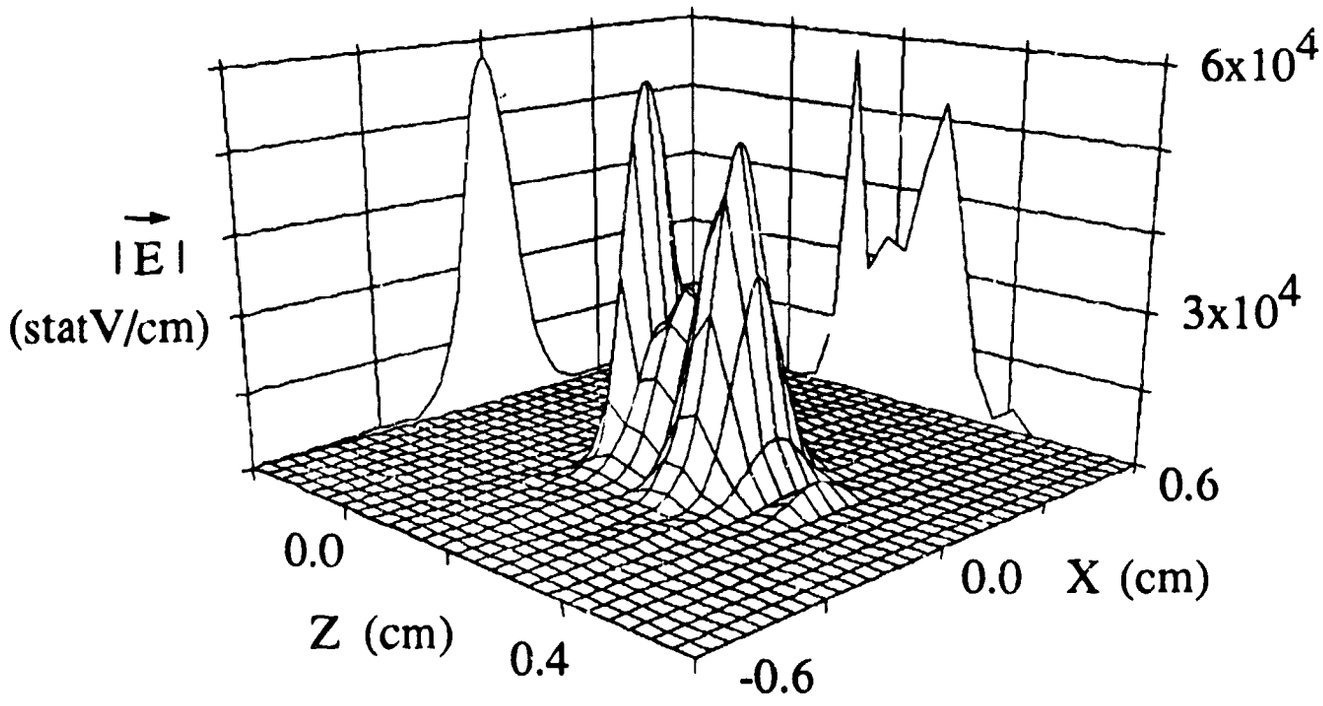
$|\vec{E}|$
(statV/cm)
6x10^4
3x10^4
0.6
0.0
0.0 X (cm)
Z (cm)
0.4
-0.6

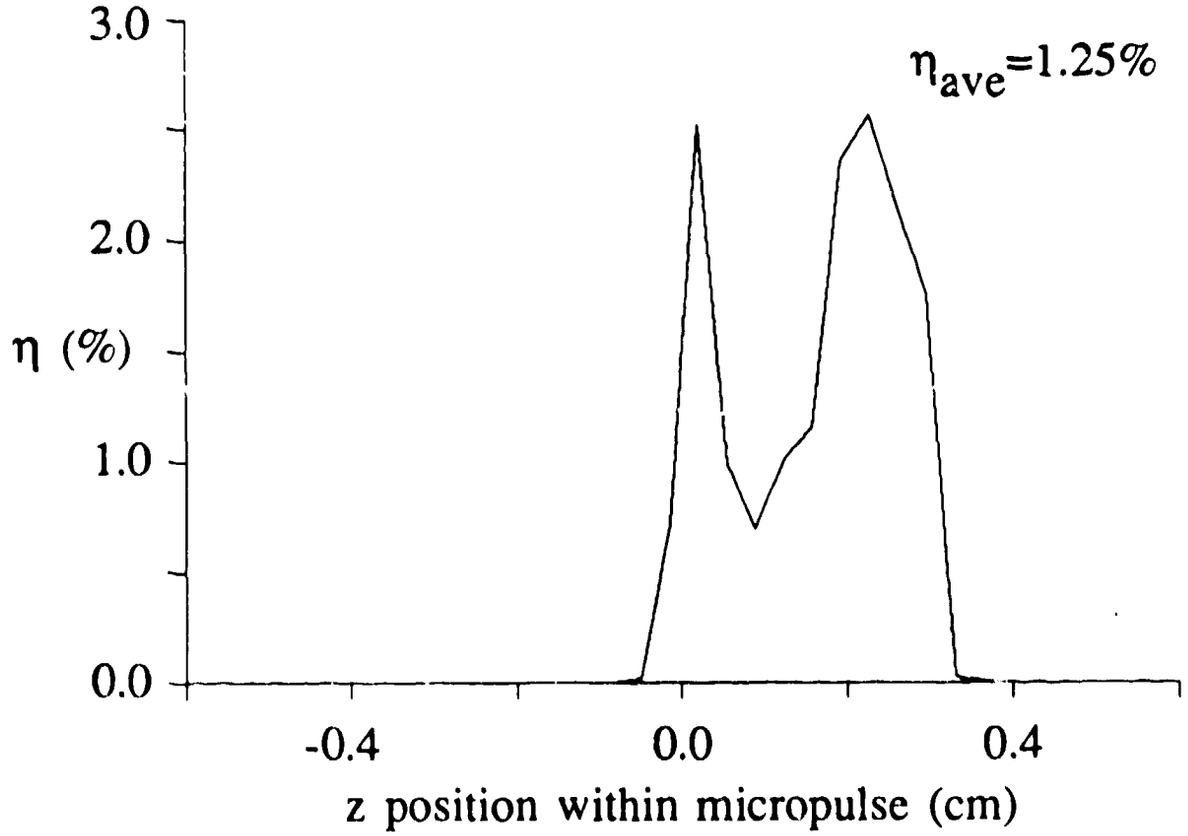
3.0
2.0
1.0
0.0
η (%)
η_{ave}=1.25%
-0.4
0.0
0.4
z position within micropulse (cm)

Figure 5

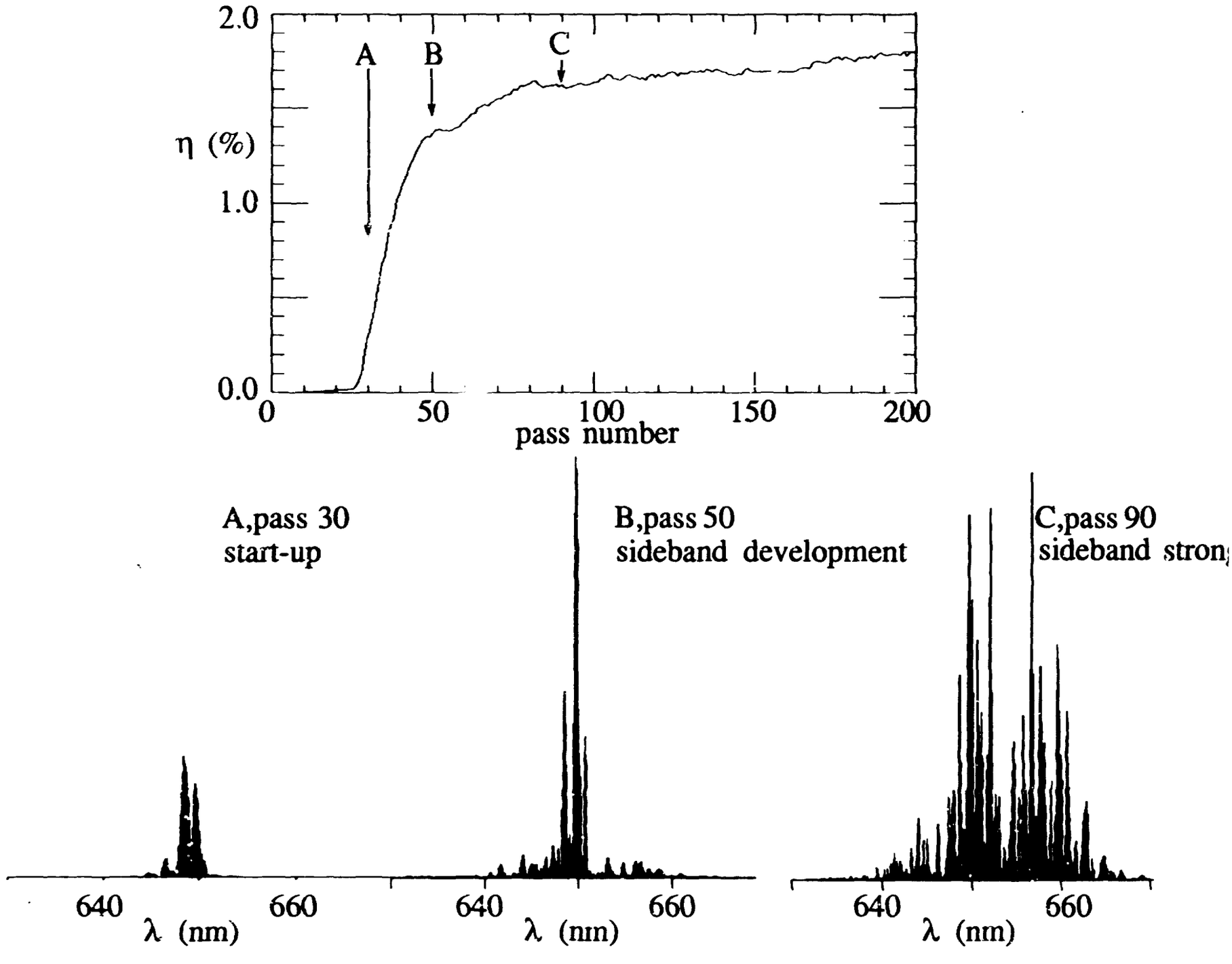
2.0
1.0
0.0
η (%)
A
B
C
0
50
100
150
200
pass number
A,pass 30
start-up
B,pass 50
sideband development
C,pass 90
sideband stron
640
660
λ (nm)
640
660
λ (nm)
640
660
λ (nm)

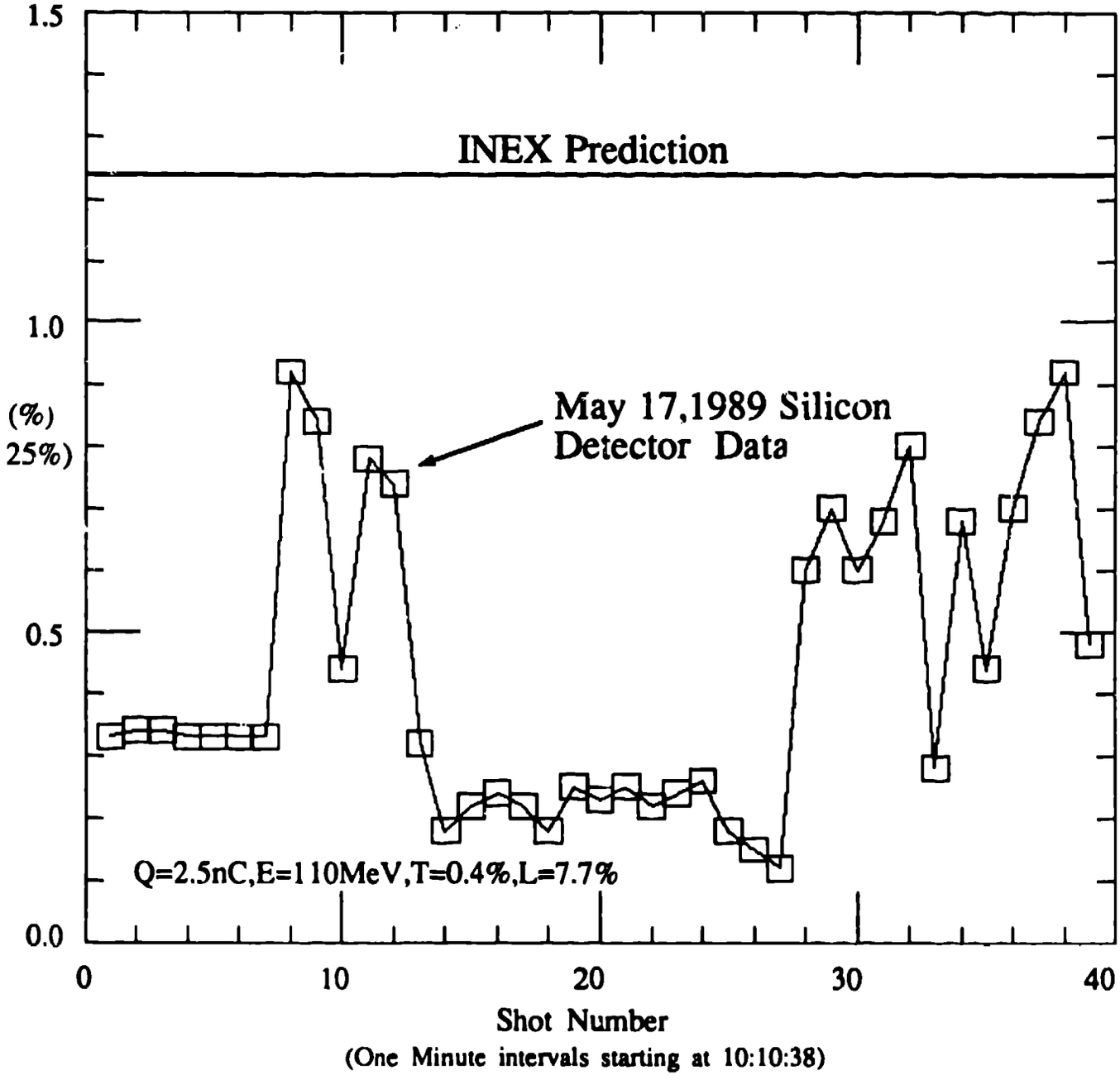
1.5
INEX Prediction
1.0
(%)
25%)
May 17,1989 Silicon
Detector Data
0.5
Q=2.5nC,E=110MeV,T=0.4%,L=7.7%
0.0
0
10
20
30
40
Shot Number
(One Minute intervals starting at 10:10:38)

Figure 7

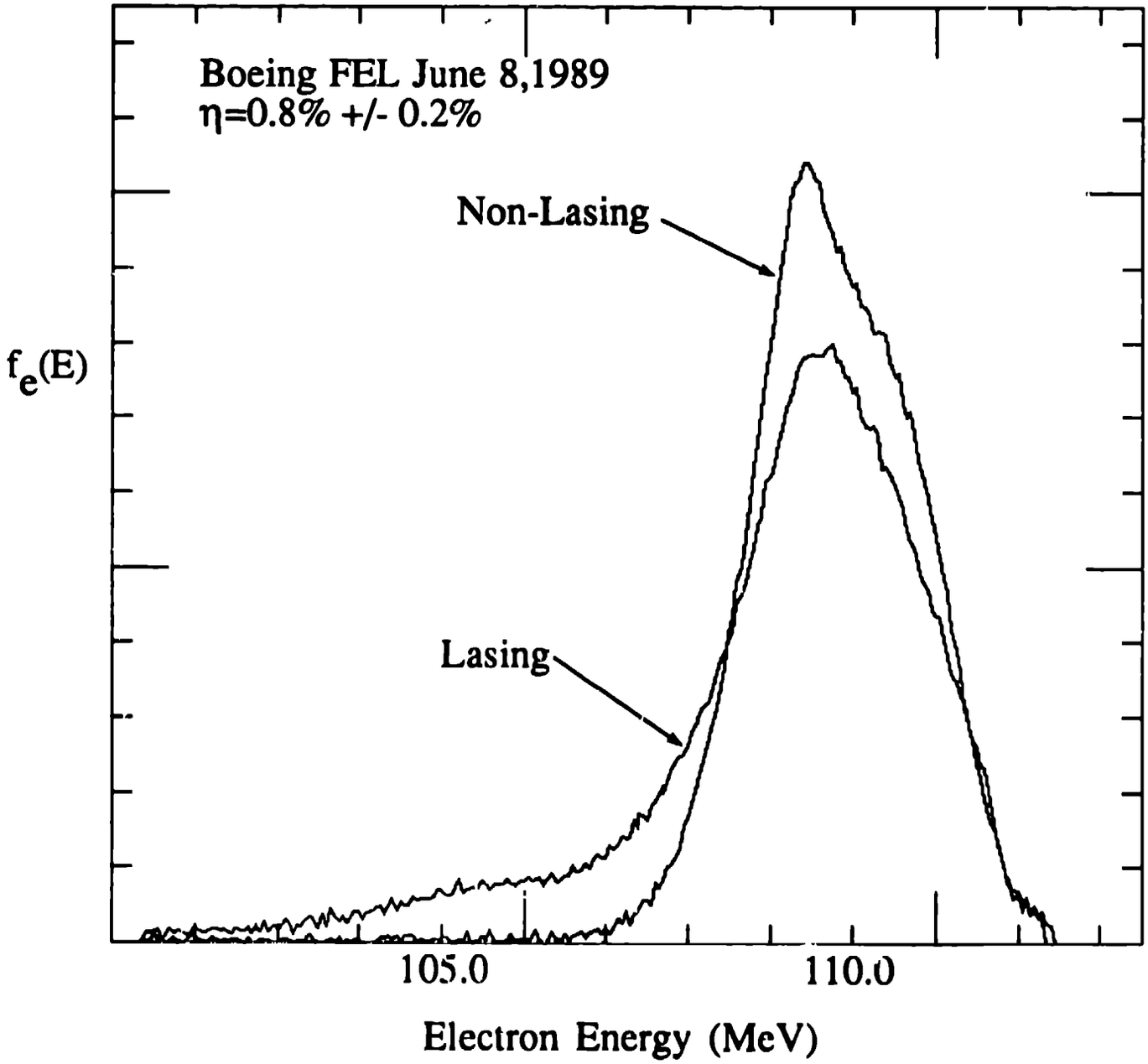
Boeing FEL June 8,1989
η=0.8% +/- 0.2%
Non-Lasing
Lasing
$f_e(E)$
105.0
110.0
Electron Energy (MeV)

Figure 8

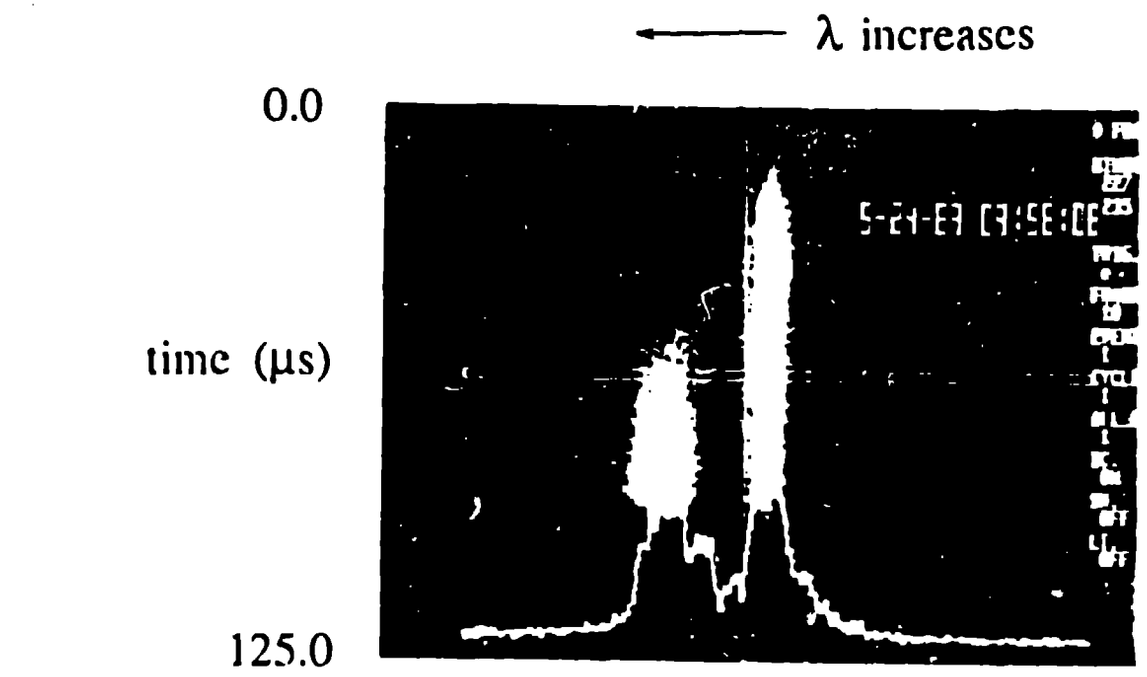
λ increases
0.0
time (μs)
125.0

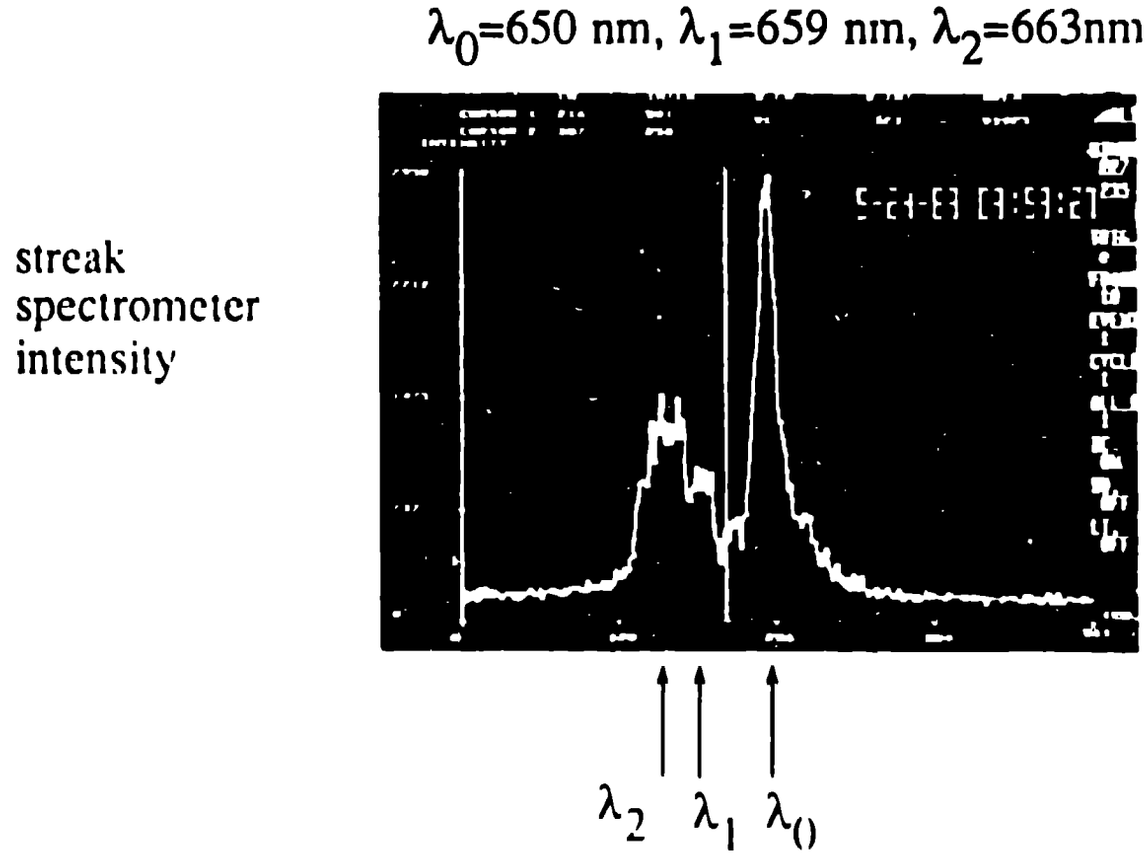
λ_0=650 nm, λ_1=659 nm, λ_2=663nm
streak
spectrometer
intensity
λ_2 λ_1 λ_0

Figure 9

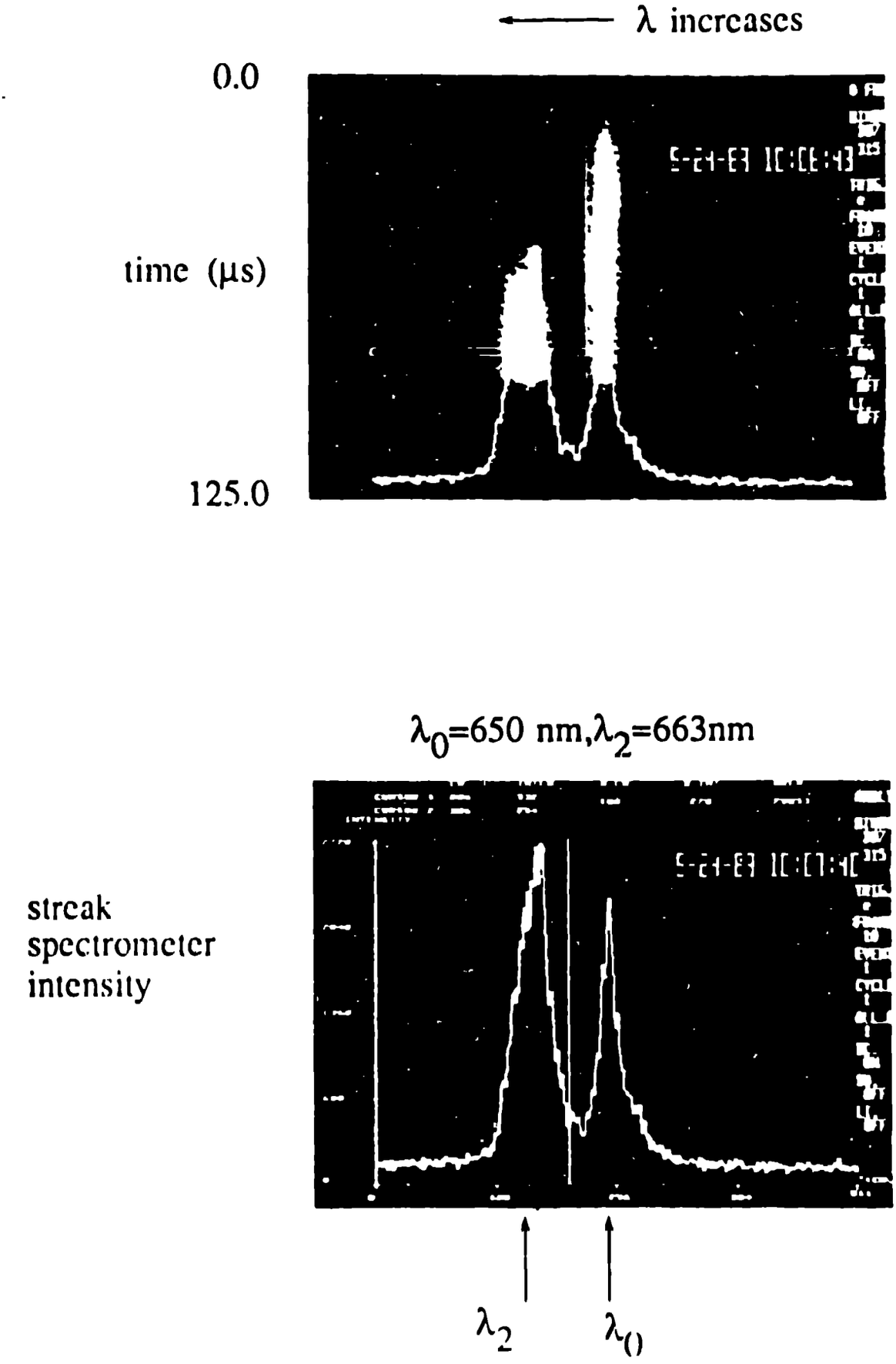
λ increases
0.0
time (μs)
125.0
λ0=650 nm,λ2=663nm
streak
spectrometer
intensity
λ2
λ0

Figure 1C

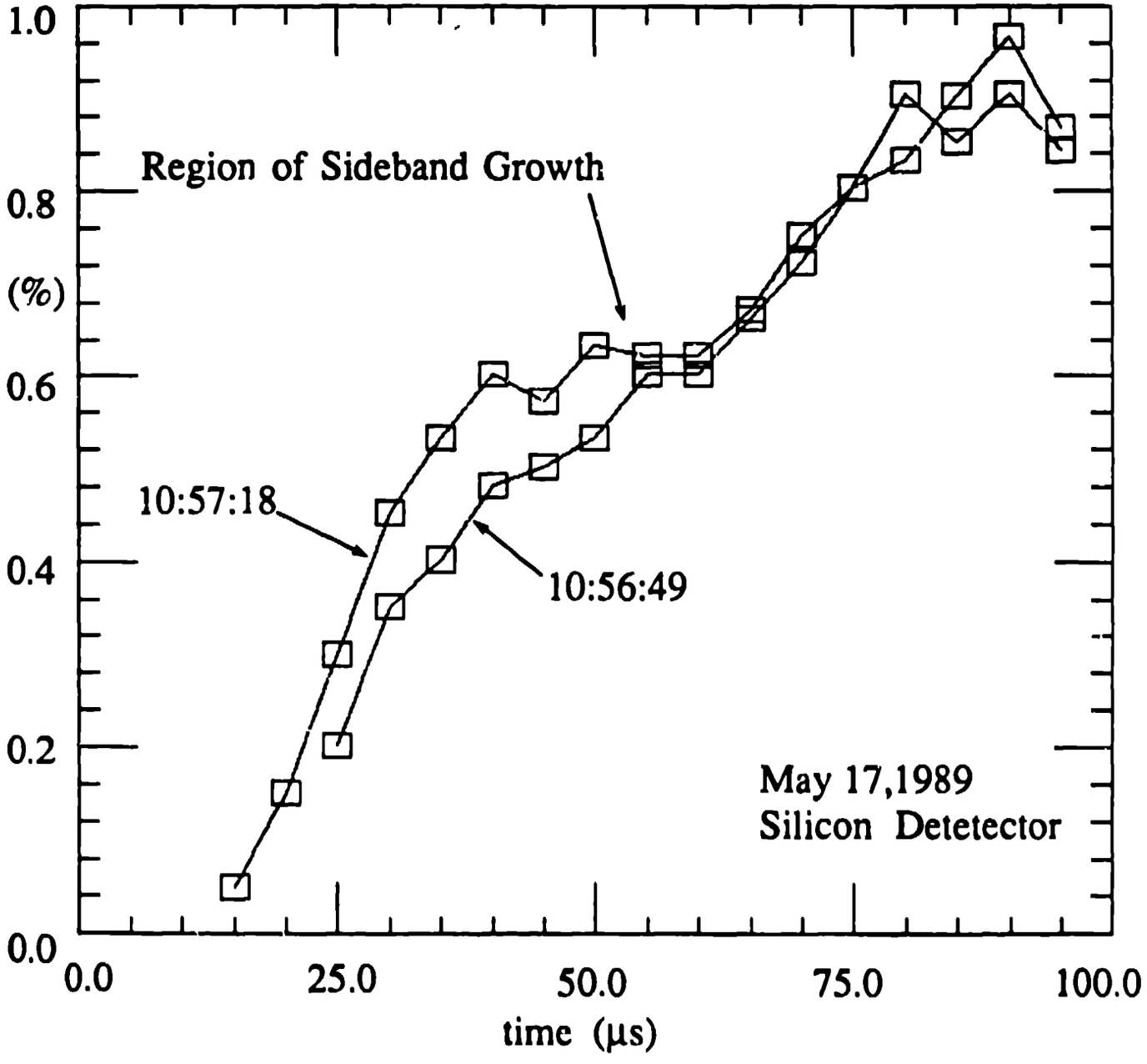
1.0
0.8
(%)
0.6
0.4
0.2
0.0
Region of Sideband Growth
10:57:18
10:56:49
May 17,1989
Silicon Detetector
0.0
25.0
50.0
75.0
100.0
time (μs)

Figure 11